# **Nanoscale**



PAPER View Article Online



Cite this: DOI: 10.1039/c8nr08647h

# Investigation of the magnetosome biomineralization in magnetotactic bacteria using graphene liquid cell – transmission electron microscopy

Emre Firlar, (1) \*a,b Meagan Ouy,a Agata Bogdanowicz,a Leigha Covnot,a Boao Song, (1) b Yash Nadkarni,a Reza Shahbazian-Yassar (1) \*b and Tolou Shokuhfar (1) \*a

Understanding the biomineralization pathways in living biological species is a grand challenge owing to the difficulties in monitoring the mineralization process at sub-nanometer scales. Here, we monitored the nucleation and growth of magnetosome nanoparticles in bacteria and in real time using a transmission electron microscope (TEM). To enable biomineralization within the bacteria, we subcultured magnetotactic bacteria grown in iron-depleted medium and then mixed them with iron-rich medium within graphene liquid cells (GLCs) right before imaging the bacteria under the microscope. Using *in situ* electron energy loss spectroscopy (EELS), the oxidation state of iron in the biomineralized magnetosome was analysed to be magnetite with trace amount of hematite. The increase of mass density of biomineralized magnetosomes as a function of incubation time indicated that the bacteria maintained their functionality during the *in situ* TEM imaging. Our results underpin that GLCs enables a new platform to observe biomineralization events in living biological species at unprecedented spatial resolution. Understanding the biomineralization processes in living organisms facilitates the design of biomimetic materials, and will enable a paradigm shift in understanding the evolution of biological species.

Received 25th October 2018, Accepted 7th December 2018 DOI: 10.1039/c8nr08647h

rsc.li/nanoscale

# Introduction

Biomineralization is the formation of minerals in living organisms. Properties of these biominerals are suitable for major medical and physical applications, which have motivated researches to biomimick these minerals.<sup>2</sup> Biomineralization has been reported to occur during the nucleation and growth of crystals, for instance, in ferritins,3 calcium carbonates,4 calcium phosphates<sup>5</sup> and magnetosomes.<sup>6</sup> Magnetosomes in the fully mature stage are magnetic magnetites, Fe<sub>3</sub>O<sub>4</sub>.<sup>1</sup> Magnetotactic bacteria are known to biomineralize magnetosomes. Due to the presence of these in vivo biomineralized magnetic particles in the cytoplasm, these bacteria align with respect to the geomagnetic field on Earth. Magnetic nanoparticles are very important for their potential uses in both medical and physical sciences. Specifically, they can be used in medical sciences as drug delivery agents, contrast enhancing tools in magnetic resonance imaging (MRI),8 and biomarkers for viruses, <sup>9</sup> bacteria<sup>10</sup> and cancer<sup>11</sup> and furthermore, in physical sciences for ferrofludics, <sup>12</sup> high density data storage<sup>13</sup> and spintronics. <sup>14</sup> Since the yield of *in vivo* biomineralized bacterial magnetosome is low for industrial applications, *in vitro* synthesis methods have to be developed to result in higher magnetosome yield while reaching the same material properties of *in vivo* biomineralized magnetosomes, such as chemical composition, magnetism and uniform size. <sup>15</sup> This makes understanding the *in vivo* magnetosome biomineralization of paramount importance.

To understand magnetosome biomineralization, several groups reported subculturing of iron deplete bacteria with iron replete medium, and observed the nucleation and growth of magnetosomes *via* time-resolved conventional transmission electron microscopy (TEM) imaging of the newly formed magnetosomes.<sup>6,16,17</sup> Baumgartner *et al.* reported that magnetite formation happens through the formation of highly disordered phosphate-rich ferric hydroxide, then its conversion into ferric (oxyhydr)oxide, and finally the formation of magnetite.<sup>16</sup> Staniland *et al.* described the formation of transient hematite and was able to observe magnetite formation after 15 minutes of iron induction through TEM and X-ray absorption spectroscopy (XAS) analyses.<sup>17</sup> Using time-resolved imaging and

<sup>&</sup>lt;sup>a</sup>University of Illinois at Chicago, Department of Bioengineering, Chicago, IL, 60607, USA. E-mail: efirlar@gmail.com

<sup>&</sup>lt;sup>b</sup>University of Illinois at Chicago, Department of Mechanical and Industrial Engineering, Chicago, IL, 60607, USA

Paper Nanoscale

chemical analysis in TEM, Firlar *et al.*<sup>6</sup> reported the presence of amorphous ferric hydroxide when magnetosomes were smaller than 10 nm, followed by partial crystallization with 2 line ferrihydrite in particles with diameter in the range of 10–15 nm. For particles with sizes larger than 15 nm, fully magnetite phase was detected. Both Staniland *et al.* and Firlar *et al.* reported the formation of hematite around magnetite as well.<sup>6,17</sup> All of these works were carried out by drying the bacteria after the desired stage of biomineralization was reached, thus imaging was executed on the dead bacteria.

In order to observe the biomineralization kinetics in living species, the bacterial culture needs to be preserved in the growth medium. Unless preserved cryogenically or as hermetically sealed via liquid cells, bacteria will be dehydrated in the TEM column, losing their native properties. Liquid-cell TEM enclosures using Si<sub>3</sub>N<sub>4</sub> membranes<sup>18</sup> and graphene monolayers<sup>19</sup> have been introduced to enable the visualization of hydrated dose sensitive samples and allow monitoring of sample specific dynamics, which is not possible with cryofixation of the samples. Si<sub>3</sub>N<sub>4</sub> membrane fluid cells involve encapsulation of samples between two electron transparent Si<sub>3</sub>N<sub>4</sub> membranes. 20,21 This technology also enables delivering liquid to the liquid cell chamber during TEM imaging, allowing to monitor dynamics relevant to reactions taking place due to the interaction of the host sample in the enclosure with the external fluid flow. 19,22-24 This technique was also employed by Woehl et al. to prove that bacteria could remain viable in TEM.25 However, Si<sub>3</sub>N<sub>4</sub> membranes are relatively thick (15-50 nm), and due to extra bowing in vacuum, the spatial resolution will be reduced significantly. In addition, their microfabrication technology is costly and difficult.<sup>26</sup> Graphene liquid cells (GLC), on the other hand, provide hermetic seal to the samples via wrapping them with two monolayers of graphene with the sample inside.<sup>27</sup> Graphene is very strong, biocompatible and electron transparent. 28-31 Furthermore, graphene scavenges reactive radicals, which form via the radiolysis during electron-sample interaction.<sup>32</sup> Whole cell imaging ability of GLCs has been reported by Park et al. by resolving viruses and cytoskeleton structure of cells.33 Bacillus subtilis was imaged using GLC-TEM by Mohanty et al. 19 Furthermore, crystal structure and chemistry of ferritin proteins were studied by Wang et al.34 In addition, by controlling the electron beam dose, it was shown that the formation of H2 and other reactants can be controlled in GLCs. 34,35

Currently, the abilities of both keeping the cells viable and having enough resolution to resolve biomineralization events in sub-nm scale concurrently are missing. Therefore, in this study we employed the GLC-TEM imaging technique to monitor the magnetosome biomineralization in magnetotactic bacteria. To achieve this, we cultured the bacterium in iron deplete growth medium. Once passed through the log-phase, induction of iron was carried out by subculturing these bacteria with iron replete growth medium. At this stage, Fe<sup>3+</sup> ions are internalized by the bacteria and formation of magnetosomes occur. Right after the initiation of subculturing, an aliquot from the bacteria culture was encapsulated in GLC

(Fig. 1a) and the formation and growth of magnetosomes were monitored in real time using TEM (Fig. 1b–d).  $^{36}$  Encapsulation of bacterial culture in graphene and preservation of growth medium surrounding the particle with intact graphene was verified via low loss electron energy loss spectroscopy (EELS). Characterization of the mature magnetosomes was carried out via iron  $L_3$  core edge EELS and formation of magnetosomes were monitored both qualitatively and quantitatively via line profiles drawn over the magnetosomes in TEM images indicating the mass-contrast progression through biomineralization.

# **Experimental**

#### Sample preparation

Magnetosprillum magneticum (ATC 700264) was used during biomineralization experiments. ATCC Medium 1653 revised magnetic spirillum growth medium (MSGM) with iron deplete medium was used to subculture them under microaerobic conditions. After the subculturing of the bacteria, for the induction experiment, ferric quinate added iron replete MSGM was used. Right after induction, GLC preparation was carried out.

#### **TEM imaging**

1  $\mu$ l sample was drop cast on 2000 mesh graphene coated copper grid (Graphene Supermarket, Graphene Laboratories Inc.) and the secondary graphene coated copper grid was added onto it forming the graphene encapsulation. TEM imaging was carried out at 80 kV using JEOL 1220 and Hitachi HT7700. Image acquisition was carried out *via* Digital Micrograph. During video recording and image acquisition, 0.1 (200 e per nm² per frame) and 1 second exposures (2000 e per nm² per frame) were used, respectively.

#### HAADF-STEM EELS

EELS analysis was carried out using Hitachi HD 2300 STEM with Gatan Enfina EELS detector. 3 mm EELS aperture and 0.1 eV per channel energy resolution were used. 159 e nm $^{-2}$  (3 ×  $10^{-6}$  s beam exposure) and 1.11 ×  $10^9$  e nm $^{-2}$  (21 s beam exposure) were used for low loss and Fe L<sub>3</sub> edges, respectively. For the L<sub>3</sub> edge, background removal was carried out with a 30 eV window in Digital Micrograph. 3 channel spectrum smoothing and reference spectra fitting to experimental Fe L<sub>3</sub> spectra was carried out in OriginPro 2016. For the analysis of the oxidation state of iron, Fe<sup>2+</sup> (octahedral), Fe<sup>3+</sup> (tetrahedral), Fe<sup>3+</sup> (octahedral) and FeO(OH) were fitted to the spectra and ratio of Fe<sup>2+</sup> (octahedral)/Fe<sup>3+</sup> (tetrahedral) + Fe<sup>3+</sup> (octahedral) was computed for the determination of the iron oxide type.

#### Fluorescence imaging

SYTO 9 and propidium iodide (Fisher Scientific Company LLC, Life Technologies L7007) was used as fluorescence stains for the investigation of bacterial viability. 0.5 µl bacteria was dropcast on glass slide and cover slip was added onto it. It is also sealed by nail polish to eliminate air flow into the medium. Fluorescence imaging was carried out using Olympus BX-51.

Nanoscale

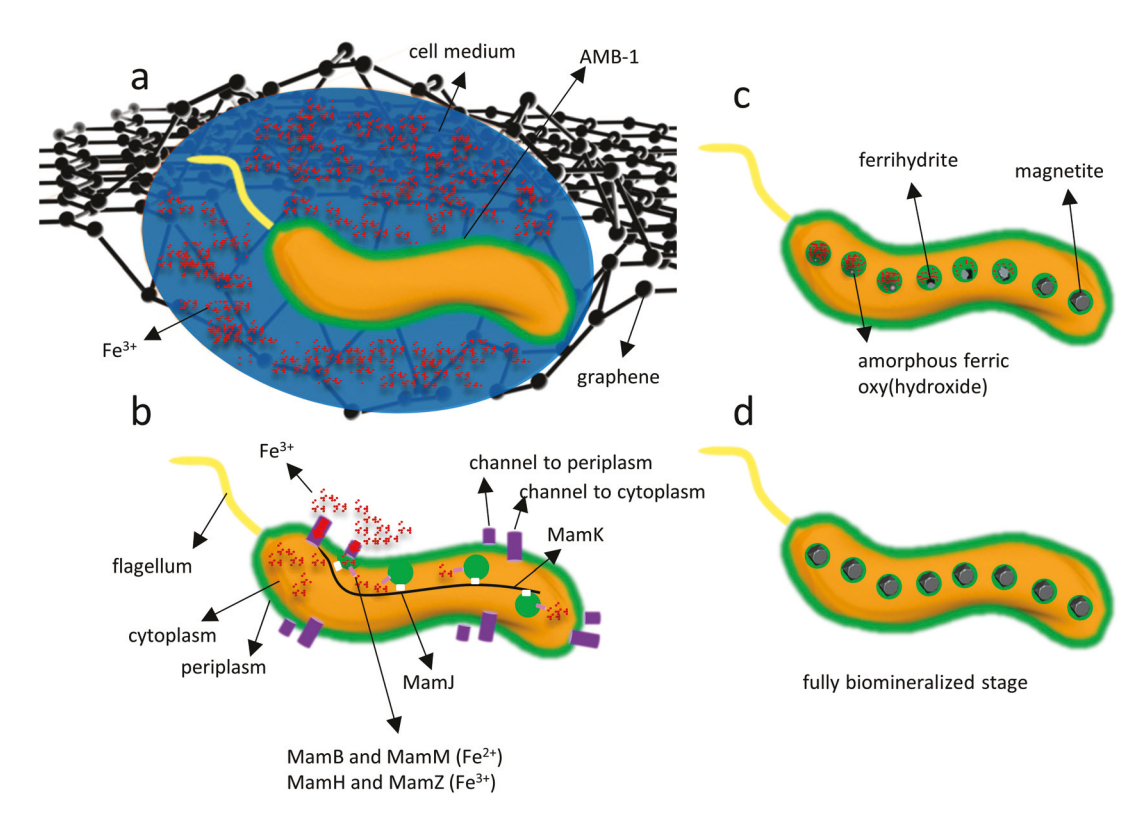


Fig. 1 (a) Schematic showing in vivo bacterial magnetosome biomineralization phenomenon in a GLC. (b) Endocytosis of iron ions (red color) through two separate channels: one into the periplasm (purple color-small) and then to the invaginated vesicles, 37,38 and the other to the cytoplasm (purple color-large), which later on goes into the vesicle through iron channels. MamB and MamM proteins control transport of Fe<sup>2+</sup> and MamH and MamZ proteins control the transport of Fe<sup>3+</sup> from the cytoplasm into the vesicles (pink color).<sup>37</sup> MamK is the protein forming filament (black color). MamJ protein controls attachment of particles onto the chain (white color). (c) Formation of iron oxides in the bacterium. Oxygen in the water based cell medium diffuses into the bacterium and causes iron oxide mineral formation.<sup>39</sup> Progression is illustrated as the particle growth from left to right in the bacterium. Mms6 proteins control the formation of magnetite crystal in the presence of iron ions (blue color). (d) Fully grown particles in each vesicle are shown in the final state of biomineralization.

### Results and discussion

Comparison of conventional and GLC-TEM imaging of magnetotactic bacteria are reported in Fig. 2a and b, respectively. Higher image contrast was reported in the conventionally imaged bacterium showing crisper details of the magnetosomes, but the bacterium in that stage is assumed to be dead due to the nature of the drop casting TEM sample preparation. Specifically, sample was let dry on the bench-top and then placed in the TEM chamber, both of which eliminates all liquid content. Because the bacterium lacks liquid content, it becomes more tolerant to electron beam induced damage. On the other hand, the bacterium in GLC enclosure is more resistant to electron beam induced radiation damage than liquid cells with Si<sub>3</sub>N<sub>4</sub> membranes. 32,34,35,40 This is because of the less thickness of both the support and the surrounding liquid, causing accumulation of less electron beam induced energy, and thus less formation of radiation by products upon electron beam exposure. Furthermore, thicker membranes, under the same electron dose and voltage cause higher radical yield and higher rate of secondary radical reactions.41 When electron overexposure is applied, the formation of hydrogen molecule bubbles is observed, 35 which is also an indication that the sample is kept in liquid environment. In this work, approximately 2000 e nm<sup>-2</sup> and 200 e nm<sup>-2</sup> was used for image acquisition and video recording, respectively, which are comparable to the electron dose used for cryo-TEM imaging.<sup>42</sup>

Verification of the intact graphene with entrapped water was done by carrying out low loss EELS. This analysis shows the presence of graphene optical gap at 6 eV, water exciton peak at 8.5 eV and graphene  $\sigma + \pi$  bond at 14 eV, as shown in Fig. 3a. These are all indications of the proper encapsulation of the bacterium in between graphene with the growth medium surrounding it, in addition to the visual confirmation reported in Fig. 2b. Further investigation of the chemistry in the mature magnetosomes was executed by iron L3 core edge EELS analysis as shown in Fig. 3b. The collected spectrum was fitted with reference spectra of Fe<sup>2+</sup> (octahedral), Fe<sup>3+</sup> (tetrahedral), Fe3+ (octahedral) and FeO(OH). The relative ratio of Fe<sup>2+</sup> to Fe<sup>3+</sup> helps to investigate the final structure of the magnetosomes when kept properly in the liquid growth medium. This ratio is calculated to be 0.35. The fact that this ratio is 0.5 for a perfect Fe<sub>3</sub>O<sub>4</sub> ([Fe<sup>2+</sup>]<sup>tet</sup>[Fe<sup>2+</sup>, Fe<sup>3+</sup>]<sup>oct</sup>), 43 the value of Fe<sup>2+</sup>/ Fe<sup>3+</sup> = 0.35 suggests two possible contributions of additional

Paper Nanoscale

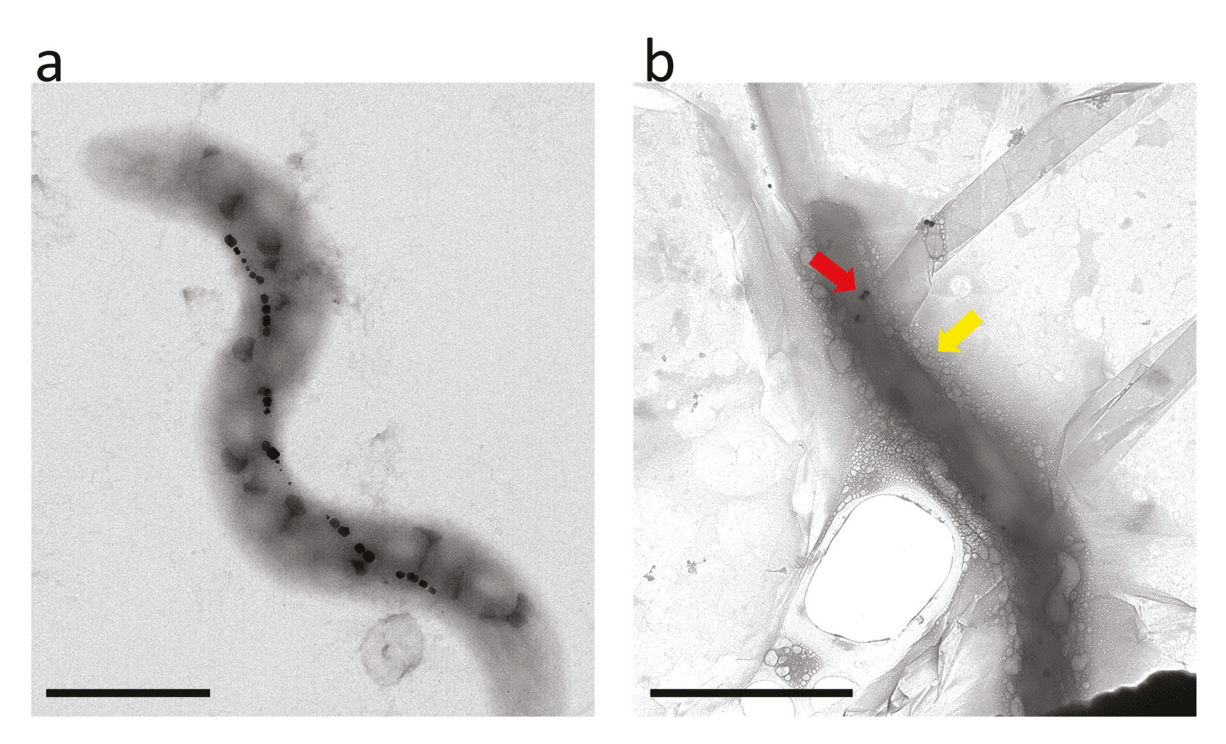


Fig. 2 Comparison of BF-TEM images of magnetotactic bacteria, which underwent biomineralization in conventional imaging and GLC imaging methods. (a) Bacteria in growth medium was drop cast on continuous carbon grid and left to dry for 5 minutes before loading to the TEM holder. Scale bar: 500 nm. (b) Bacteria was encapsulated in GLC and directly loaded into the TEM holder. Red arrows show magnetosomes and the yellow arrow in GLC shows the presence of hydrogen molecule bubbles formed via electron over exposure. Scale bar: 1000 µm.

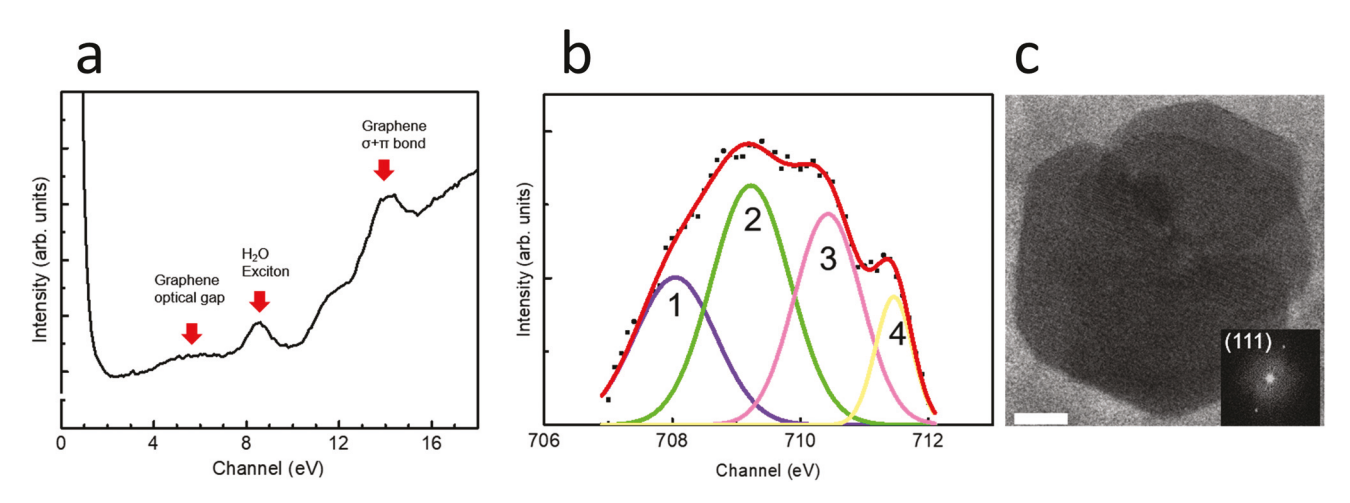


Fig. 3 (a) Low loss EELS collected at close proximity of magnetotactic bacterium encapsulated within graphene liquid cell. Fingerprints for graphene and water show proper bacterial sample preservation in between layers of graphene. (b) Fe  $L_3$  core EEL spectrum collected from mature magnetosomes. The ratio of the areas between peak 1 to peaks (2 + 3), corresponding to  $Fe^{2+}$  (octahedral) to  $Fe^{3+}$  (tetrahedral + octahedral) ratio, is 0.35. Peak 4 is attributed to FeO(OH). (c) BF-STEM image collected from three overlapping magnetosomes showing  $Fe_3O_4$  (111) interplanar spacing in the FFT collected (inset). Scale bar: 10 nm.

 ${\rm Fe}^{3+}$  to this ratio: (i) presence of another iron oxide, which contributes to a higher percentage of  ${\rm Fe}^{3+}$ ; (ii) little amount of  ${\rm Fe}^{3+}$  is present in the extracellular region of bacterium. Specifically, 2 ml ferric quinate (0.01 M, that is, 0.27 g  ${\rm FeCl}_3$  and 0.17 g quinic acid in 100 ml  ${\rm H}_2{\rm O}$ ) was added into 1 liter of growth medium to obtain the iron rich growth medium. During iron induction, 18 ml bacteria culture was subcultured

with 6 ml iron rich growth medium. Furthermore, the tightly packing nature of graphene encapsulation due to van der Waals forces suggests that the medium surrounding the bacterium is thin. Therefore, contribution of Fe<sup>3+</sup> in the extracellular region to the Fe<sup>3+</sup> EELS L<sub>3</sub> signal obtained from individual mangetosome is considered negligible. As suggested earlier by Firlar *et al.*<sup>6</sup> through Gibbs free energy calculations, magnetite

Nanoscale

may have been oxidized to hematite, supporting the first possibility. This occurs first by the conversion of magnetite to maghemite and furthermore to hematite spontaneously, which may have caused the Fe<sup>2+</sup>/Fe<sup>3+</sup> ratio to deviate from 0.5.  $\Delta H_f^{\circ}$  for magnetite, maghemite, hematite and oxygen are -1118.4, 44 -809.0, 44 -824.2 (ref. 44) and 0 kJ mol<sup>-1</sup>, 45 respectively, and  $S_{298}^{\circ}$  for magnetite, maghemite, hematite and oxygen are 146.4, 44 102.4, 44 87.4 (ref. 44) and 205.0 J (mol °K)<sup>-1</sup>, 45 respectively. The conversion of magnetite to maghemite and furthermore to hematite are defined by eqn (1) and (2),

$$2\text{Fe}_3\text{O}_4 + 0.5\text{O}_2 \to 3\gamma\text{-Fe}_2\text{O}_3 \quad \Delta G = -1630 \text{ kJ mol}^{-1} \quad (1)$$

$$\gamma$$
-Fe<sub>2</sub>O<sub>3</sub>  $\rightarrow \alpha$ -Fe<sub>2</sub>O<sub>3</sub>  $\Delta G = -11 \pm 2$ kJ mol<sup>-1</sup> (2)

showing the spontaneous conversion of magnetite to maghemite and hematite. Even though graphene liquid cells reduce the amount of beam induced radicals forming in solution, one should further study the effect of oxidizing radicals, oxygen gas, and reducing radicals formations during imaging. It is possible these radicals could change the oxidation state of iron during EELS spectrum acquisition.

On a separate magnetosome, the bright field STEM image collected showed lattice fringes referring to magnetite (111) through fast Fourier transformation (FFT) analysis (Fig. 3c). Furthermore, this shows that not all the magnetosomes have the hematite layer as discussed above.

In order to achieve time resolved monitoring of magnetosome nucleation and growth, iron replete growth medium was mixed with the bacteria in iron deplete growth medium (t = 0 s). The bacteria in growth medium was sandwiched between monolayers of graphene to form GLC, and the first image of the bacterium was recorded at t = 70 minutes after induction and is reported Fig. 4a. Red arrow indicates the MamK which is actin-like protein. As given in Uebe and Schüler,<sup>37</sup> with the polymerization of MamK, filament form and with the interaction of this filament and MamI on the

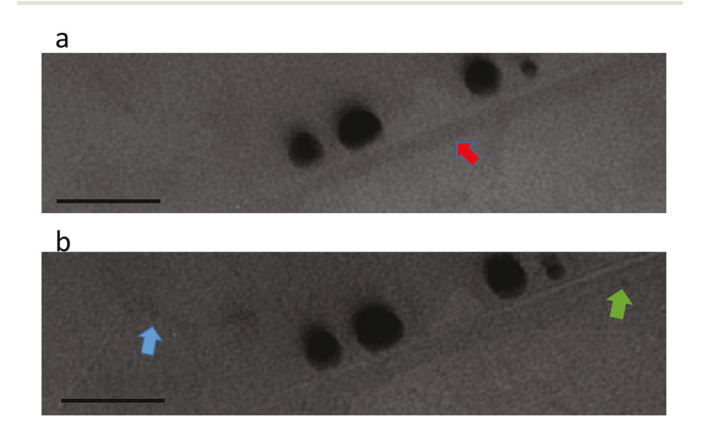


Fig. 4 TEM images of magnetotactic bacterium grown in iron depleted growth medium, mixed with iron replete growth medium, and encapsulated in GLC. Red arrow shows MamK. Blue and green arrows indicate formation of magnetosomes. (a) 70 min after GLC encapsulation and (b) 115 min after GLC encapsulation. Scale bar: 50 nm.

magnetosome, magnetosomes are aligned into chains. Residual magnetosomes were reported to be present due to the small quantity iron present in the iron deplete medium. In vivo biomineralization was observed by the sequential imaging. Specifically, the image recorded at t = 115 minutes is reported in Fig. 4b. Nucleation and growth of the two magnetosomes with sizes around 4 nm are observed, as marked with the blue and green arrows. More than 70% bacterial viability was reported using fluorescence imaging before the induction was carried out. De Jonge and Peckys<sup>46</sup> indicated that fluorescence live/dead assay could not be considered the proper way for cell viability measurement, cells could be dead even due to electron-bacteria interaction without the deterioration of the cell wall, which would prevent the entry of the red dye into the bacteria. A more reliable way to measure the cell viability suggested by the same group was to monitor the cellular functions during in situ TEM, which they reported to be not feasible. As a response to that work, Kennedy later showed the expression of LuxI-LVA after the induction of *E. coli* with isopropyl β-D-1-thiogalactopyranoside (IPTG) during in situ STEM. 47 Very recently, Firlar et al. also monitored live insulin secretion from pancreatic beta cells using GLC-TEM. 48 In addition to fluorescence imaging for viability examination, they also reported insulin secretion and exocytosis which only occur when the pancreatic islet cells are viable. In this work, the in vivo biomineralization, which only happens when the bacteria are alive, indicates that these bacteria were still viable during GLC-TEM imaging when exposed to 200 e nm<sup>-2</sup> per frame during video recording and 2000 e nm<sup>-2</sup> during image acquisition.

TEM images in Fig. 5a and c were taken after 17 minutes of iron induction and shows a bacterium wrapped in GLC. As discussed earlier, the surrounding bubbles indicate the formation of H2 molecules in growth medium due to the electron induced radiolysis. TEM images in Fig. 5b and d show the bacterium image after 31 minutes of iron induction. An increase in the image contrast is visible by comparing the magnetosome image intensity in Fig. 5c and d, which was further quantified by the line profile comparison across the magnetosome at two time stamps in Fig. 5e. The green rectangles drawn on the profiles show the contrast increase for the magnetosome imaged after 31 minutes of induction. This indicates that the mass density of magnetosomes increases pointing to an increase in the formation of Fe<sub>3</sub>O<sub>4</sub> phase. This can further be elaborated with the image contrast analysis using eqn (3).

$$C = \frac{\Delta I}{I_{\rm b}} = \frac{I_{\rm s} - I_{\rm b}}{I_{\rm b}} = \frac{\Delta t \times N_0 \times \sigma \times \rho}{A} \tag{3}$$

where C,  $I_{\rm b}$ ,  $I_{\rm s}$ ,  $\Delta t$ ,  $N_0$ ,  $\sigma$ ,  $\rho$  and A are contrast, background image intensity, feature image intensity, thickness difference, Avogadro's number, elastic scattering cross section, density and molecular weight, respectively. Using eqn (3) for the particles in Fig. 5c and d, the contrast increases in the 14 minutes Paper Nanoscale

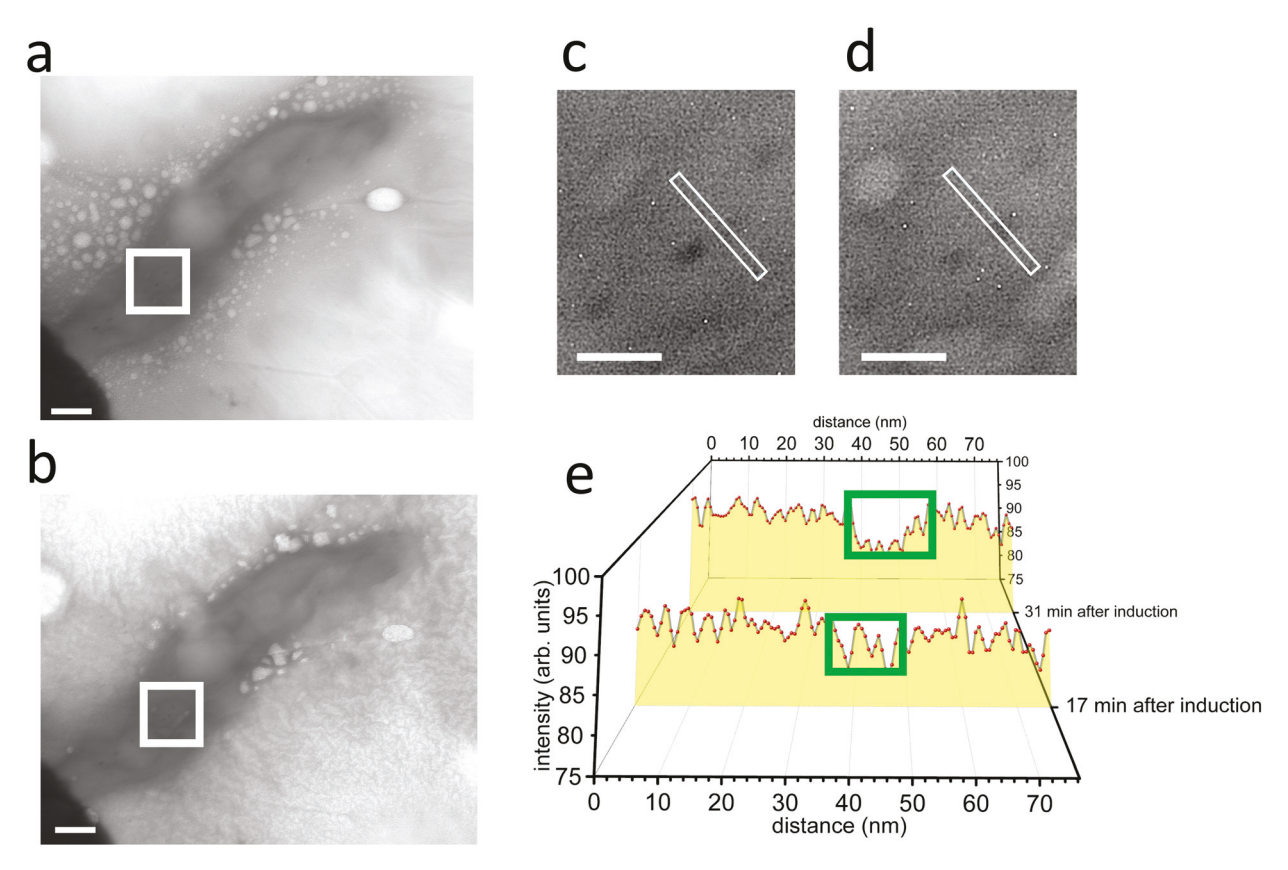


Fig. 5 TEM images showing an increase in image contrast throughout the biomineralization event in the same bacterium encapsulated within GLC. (a) t = 17 minutes after induction, and (b) t = 31 minutes after induction. Scale bar: 200 nm. Zoomed in images with the line profiles drawn across individual magnetosomes are shown in (c) for the marked square in (a), and (d) for the marked square in (b). Scale bar: 50 nm (e) the comparison of image contrast evolution in magnetosomes. Higher contrast for the magnetosome imaged after 31 minutes induction indicates the progress of biomineralization event.

course of biomineralization, this in turn resulted in thicknesses, calculated using eqn (4),

$$\Delta t = \frac{A \times C}{N_0 \times \sigma \times \rho} \tag{4}$$

Alternatively, this change in image contrast could be due to the increase in mass density of the particle over time, which is known to progress from 4.2 (ref. 49) (ferric oxyhydroxide) to 5.2 (ref. 50) (magnetite) g cm<sup>-3</sup>. For the complex nature of the analysis, we have not taken into account the particle rotation and diffraction contrast effects, which may have further affected the observed contrast change. So, the increase in image contrast in the magnetosome during TEM imaging as a function of incubation time indicates progression of the biomineralization event either through an increase in thickness or an increase in density.

Several models were put forward for the elucidation of magnetosome biomineralization. Schüler *et al.*<sup>51</sup> claimed that Fe<sup>3+</sup> is internalized and reduces to Fe<sup>2+</sup>. Then, Fe<sup>2+</sup> reoxidizes to first form low density hydrous oxide, and then to high density ferrihydrite. Finally, one third of Fe<sup>3+</sup> is converted to Fe<sup>2+</sup> to form magnetite. Jogler and Schüler<sup>52</sup> stated that iron is internalized and due to its supersaturation in the cytoplasm, it is

encapsulated into the already formed magnetosome vesicles by MamB and MamM proteins, or iron is sent from the periplasm to the vesicles directly by the same proteins. Partial reoxidization of iron caused by MamT causes the formation of high activity ferric oxide, which may further react with dissolved Fe<sup>2+</sup> forming magnetite. Arakaki *et al.*<sup>36</sup> suggested that magnetosome membrane invaginations from the cytoplasmic membrane occur first, with the arrangement of these along with cytoskeletal filaments, and then external iron is transported into the vesicles by transmembrane proteins and magnetite crystal formation by magnetosome proteins.

# Conclusions

In this work, we demonstrated the *in vivo* magnetosome biomineralization events in magnetotactic bacteria in liquid environment using GLC-TEM imaging. Usage of graphene layers instead of two relatively thicker Si<sub>3</sub>N<sub>4</sub> membranes in fluid cell TEM holder enabled us to resolve sub 10 nm magnetosomes. To initiate the biomineralization, bacteria grown in iron deplete medium was subcultured with iron replete growth medium and wrapped in between graphene monolayers. The

Nanoscale Paper

intactness of graphene and presence of water were monitored by examining the fingerprints for graphene and water in low loss EELS, respectively. The final chemical composition and crystal structure of biomineralized magnetosome were characterized via the analysis of Fe L3 edge and bright field STEM imaging, respectively, and found to be magnetite with some magnetosomes having a trace amount of hematite. The enhancement of the contrast profile in TEM images indicated the progression of biomineralization due to the accumulation of more magnetite in the magnetosomes increasing the massthickness contrast. Our finding on the progress of the biomineralization process is a good indication that the bacteria were viable and maintained their cellular activities during TEM imaging. To the best of our knowledge, this is the first study showing the applicability of GLCs for in vivo biomineralization events in TEM. These results are of utmost importance to the biomaterials and biological community as our work introduces a new platform to investigate the in vivo biomineralization in living biological organisms.

# Conflicts of interest

There are no conflicts to declare.

# Acknowledgements

T. Shokuhfar is grateful to the NSF CAREER Award DMR-1564950. R. Shahbazian-Yassar acknowledges the financial support from NSF-DMR Award number 1710049. The electron microscopy costs were supported by the Chicago Biomedical Consortium Award PDR-086. Fluorescence and TEM imaging work made use of instruments in the Electron Microscopy Service (Research Resources Center, UIC). STEM imaging, STEM-EDS and STEM-EELS work made use of the EPIC facility of Northwestern University's NUANCE Center, which has received support from the Soft and Hybrid Nanotechnology Experimental (SHyNE) Resource (NSF ECCS-1542205); the MRSEC program (NSF DMR-1121262) at the Materials Research Center; the International Institute for Nanotechnology (IIN); the Keck Foundation; and the State of Illinois, through the IIN.

# References

- 1 A. Lia and W. Stephen, Angew. Chem., Int. Ed., 2003, 31,
- 2 S. Mann, J. Mater. Chem., 1995, 5, 935-946.
- 3 P. J. Artymiuk, E. R. Bauminger, P. M. Harrison, D. M. Lawson, I. Nowik, A. Treffry and S. J. Yewdall, in Ferritin: A Model System for Iron Biomineralization BT – Iron Biominerals, ed. R. B. Frankel and R. P. Blakemore, Springer US, Boston, MA, 1991, pp. 269-294.
- 4 N. K. Dhami, M. S. Reddy, M. S. Mukherjee and A. Mukherjee, Front. Microbiol., 2013, 4, 314.

- 5 C. Chi, Y. Shi, H. Zheng, Y. Zhang, W. Chen, W. Yang and Y. Tang, Mater. Chem. Phys., 2009, 115, 808-814.
- 6 E. Firlar, T. Perez-Gonzalez, A. Olszewska, D. Faivre and T. Prozorov, J. Mater. Res., 2016, 31, 547-555.
- 7 S. C. McBain, H. H. P. Yiu and J. Dobson, Int. J. Nanomed., 2008, 3, 169-180.
- 8 D. E. Sosnovik, M. Nahrendorf and R. Weissleder, Basic Res. Cardiol., 2008, 103, 122-130.
- 9 P. Michalek, S. Dostalova, H. Buchtelova, N. Cernei, L. Krejcova, D. Hynek, V. Milosavljevic, A. M. J. Jimenez, P. Kopel, Z. Heger and V. Adam, Electrophoresis, 2016, 37, 2025-2035.
- 10 K. Cihalova, D. Hegerova, A. M. Jimenez Jimenez, V. Milosavljevic, J. Kudr, S. Skalickova, D. Hynek, P. Kopel, M. Vaculovicova and V. Adam, J. Pharm. Biomed. Anal., 2017, 134, 325-332.
- 11 O. Zitka, S. Krizkova, L. Krejcova, D. Hynek, J. Gumulec, M. Masarik, J. Sochor, V. Adam, J. Hubalek, L. Trnkova and R. Kizek, Electrophoresis, 2011, 32, 3207-3220.
- 12 W. Li, Z. Liang, Z. Lu, X. Tao, K. Liu, H. Yao and Y. Cui, Nano Lett., 2015, 15, 7394-7399.
- Singamaneni, V. N. Bliznyuk, C. Binek and E. Y. Tsymbal, J. Mater. Chem., 2011, 21, 16819-16845.
- 14 J.-P. Cleuziou, W. Wernsdorfer, T. Ondarçuhu and M. Monthioux, ACS Nano, 2011, 5, 2348-2355.
- 15 C. Valverde-Tercedor, M. Montalbán-López, T. Perez-Gonzalez, M. S. Sanchez-Quesada, T. Prozorov, E. Pineda-Molina, M. A. Fernandez-Vivas, A. B. Rodriguez-Navarro, D. Trubitsyn, D. A. Bazylinski and C. Jimenez-Lopez, Appl. Microbiol. Biotechnol., 2015, 99, 5109-5121.
- 16 J. Baumgartner, G. Morin, N. Menguy, T. Perez Gonzalez, M. Widdrat, J. Cosmidis and D. Faivre, Proc. Natl. Acad. Sci. U. S. A., 2013, 110, 14883-14888.
- 17 S. Staniland, B. Ward, A. Harrison, G. van der Laan and N. Telling, Proc. Natl. Acad. Sci. U. S. A., 2007, 104, 19524-
- 18 M. J. Williamson, R. M. Tromp, P. M. Vereecken, R. Hull and F. M. Ross, Nat. Mater., 2003, 2, 532.
- 19 N. Mohanty, M. Fahrenholtz, A. Nagaraja, D. Boyle and V. Berry, Nano Lett., 2011, 11, 1270-1275.
- 20 J. M. Grogan and H. H. Bau, J. Microelectromech. Syst., 2010, 19,885-894.
- 21 H. M. Zheng, R. K. Smith, Y. W. Jun, C. Kisielowski, U. Dahmen and A. P. Alivisatos, Science, 2009, 324, 1309-1312.
- 22 K. He, A. Nie, Y. Yuan, S. M. Ghodsi, B. Song, E. Firlar, J. Lu, Y. Lu, T. Shokuhfar, C. M. Megaridis and R. Shahbazian-Yassar, ACS Appl. Nano Mater., 2018, 1(10),
- 23 B. Song, K. He, Y. Yuan, S. Sharifi-Asl, M. Cheng, J. Lu, W. A. Saidi and R. Shahbazian-Yassar, Nanoscale, 2018, 10, 15809-15818.
- 24 K. He, X. Bi, Y. Yuan, T. Foroozan, B. Song, K. Amine, J. Lu and R. Shahbazian-Yassar, Nano Energy, 2018, 49, 338-345.
- 25 T. J. Woehl, S. Kashyap, E. Firlar, T. Perez-Gonzalez, D. Faivre, D. Trubitsyn, D. A. Bazylinski and T. Prozorov, Sci. Rep., 2014, 4, 6854.

Paper

26 S. W. Chee, S. H. Pratt, K. Hattar, D. Duquette, F. M. Ross and R. Hull, *Chem. Commun.*, 2015, **51**, 168–171.

- 27 J. M. Yuk, J. Park, P. Ercius, K. Kim, D. J. Hellebusch, M. F. Crommie, J. Y. Lee, A. Zettl and A. P. Alivisatos, *Science*, 2012, 336, 61–64.
- 28 Y. D. Kim, H. Kim, Y. Cho, J. H. Ryoo, C.-H. Park, P. Kim, Y. S. Kim, S. Lee, Y. Li, S.-N. Park, Y. Shim Yoo, D. Yoon, V. E. Dorgan, E. Pop, T. F. Heinz, J. Hone, S.-H. Chun, H. Cheong, S. W. Lee, M.-H. Bae and Y. D. Park, *Nat. Nanotechnol.*, 2015, 10, 676–681.
- 29 R. R. Nair, S. Anissimova, R. Zan, P. Blake, J. R. Blake, A. K. Geim, U. Bangert, A. P. Golovanov, S. V. Morozov, K. S. Novoselov and T. Latychevskaia, *IEEE Trans. Inf. Theory*, 1993, 39, 1057–1064.
- 30 C. Heo, J. Yoo, S. Lee, A. Jo, S. Jung, H. Yoo, Y. H. Lee and M. Suh, *Biomaterials*, 2011, 32, 19–27.
- 31 J. H. Warner, F. Schaffel, M. Rummeli and A. Bachmatiuk, *Graphene: Fundamentals and emergent applications*, Elsevier Science, 2012.
- 32 H. Cho, M. R. Jones, S. C. Nguyen, M. R. Hauwiller, A. Zettl and A. P. Alivisatos, *Nano Lett.*, 2017, 17, 414–420.
- 33 J. Park, H. Park, P. Ercius, A. F. Pegoraro, C. Xu, J. W. Kim, S. H. Han and D. A. Weitz, *Nano Lett.*, 2015, 15, 4737–4744.
- 34 C. Wang, Q. Qiao, T. Shokuhfar and R. F. Klie, *Adv. Mater.*, 2014, 26, 3410–3414.
- 35 C. Wang, T. Shokuhfar and R. F. Klie, *Adv. Mater.*, 2016, 28, 7716–7722.
- 36 A. Arakaki, H. Nakazawa, M. Nemoto, T. Mori and T. Matsunaga, J. R. Soc., Interface, 2008, 5, 977–999.
- 37 R. Uebe and D. Schüler, Nat. Rev. Microbiol., 2016, 14, 621.
- 38 A. Komeili, Z. Li, D. K. Newman and G. J. Jensen, *Science*, 2006, 311, 242–245.

- 39 K. W. Mandernack, D. A. Bazylinski, W. C. Shanks and T. D. Bullen, *Science*, 1999, 285, 1892–1896.
- 40 R. Zan, Q. M. Ramasse, R. Jalil, T. Georgiou, U. Bangert and K. S. Novoselov, *ACS Nano*, 2013, 7, 10167–10174.
- 41 T. J. Woehl and P. Abellan, *J. Microsc.*, 2017, **265**, 135–147.
- 42 J. Evans, in *Low-Dose Imaging Techniques for Transmission Electron Microscopy*, ed. K. Maaz, InTech, Rijeka, 2012, ch. 5.
- 43 F. C. Jentoft, Advances in Catalysis, Elsevier Science, 2015.
- 44 A. S. Casparian and G. Sirokman, *Chemistry for Environmental Engineering*, Momentum Press, 2015.
- 45 Standard Enthalpies, Free Energies of Formation, Standard Entropies, http://www.vias.org/genchem/standard\_enthalpies\_table.html, (accessed 2 August 2018).
- 46 N. De Jonge and D. B. Peckys, *ACS Nano*, 2016, **10**, 9061–9063.
- 47 E. Kennedy, E. M. Nelson, J. Damiano and G. Timp, *ACS Nano*, 2017, **11**, 3–7.
- 48 E. Firlar, S. Shafiee, M. Ouy, Y. Xing, D. Lee, A. Chan, S. Afelik, R. Shahbazian Yassar, Y. Wang, J. Oberholzer and T. Shokuhfar, *Microsc. Microanal.*, 2017, 23, 1310–1311.
- 49 T. Hiemstra and W. H. Van Riemsdijk, *Geochim. Cosmochim. Acta*, 2009, 73, 4423–4436.
- 50 M. Dentith and S. T. Mudge, Geophysics for the Mineral Exploration Geoscientist, Cambridge University Press, Cambridge, 2014.
- 51 D. Schüler, Int. Microbiol., 2002, 5, 209-214.
- 52 C. Jogler and D. Schüler, in *Genetic Analysis of Magnetosome Biomineralization BT Magnetoreception and Magnetosomes in Bacteria*, ed. D. Schüler, Springer Berlin Heidelberg, Berlin, Heidelberg, 2007, pp. 133–161.